

# Rough surface interferometry at 10.6 $\mu\text{m}$

Osuk Kwon, J. C. Wyant, and C. R. Hayslett

**An IR Twyman-Green interferometer is described. It uses a cw CO<sub>2</sub> laser as a light source operating at a 10.6- $\mu\text{m}$  wavelength. Theoretical analysis and experimental measurements of the relationship between the contrast of the interference fringes and the rms roughness of test surfaces are discussed. Interferometric testing results and special alignment methods are shown for rough surface optics.**

## I. Introduction

Long-wavelength interferometers,<sup>1,2</sup> especially at a wavelength of 10.6  $\mu\text{m}$ , have been used since Munnerlyn and Latta<sup>3</sup> performed rough surface interferometry about a decade ago. Infrared interferometry is useful in the fabrication and testing of optical components in high energy laser systems, modern astronomical telescopes or tracking systems, and other optical systems that require aspherics, IR optics, optically rough surfaces, and other oddly shaped optics. The remarkable research and development during the past decade in the areas of good quality CO<sub>2</sub> lasers, IR materials, and detectors have made it possible to perform better IR interferometric testing.

Long-wavelength interferometry is of interest for several reasons. First, it makes it possible to test IR transmitting materials. Second, as the aspheric departure from the best-fit reference sphere (in units of the probing wavelength) is reduced, long-wavelength interferometry is useful in obtaining interferograms of deep aspherics. Third, the specular component of the scattered light increases with increasing wavelength for randomly rough surfaces. Therefore, we can use a long-wavelength interferometer to obtain good contrast fringes when testing optically rough surfaces. It is this third application of long-wavelength interferometry that is discussed in this paper.

## II. Infrared Twyman-Green Interferometer

In the design and use of an IR Twyman-Green interferometer, compactness is a desirable feature. With this thought in mind, the interferometer was designed and constructed as shown in Figs. 1(a) and (b). A tripod base with a heavy-duty Klinger XYZ microstage supports the interferometer. A Sylvania 941S CO<sub>2</sub> laser operating at a 10.6- $\mu\text{m}$  wavelength with continuous 3-W output power is used as a coherent light source. It is a highly stable TEM<sub>00</sub> single longitudinal mode laser that has excellent coherence properties for use in an unequal path Twyman-Green interferometer. The beam is vertically polarized with a beam diameter of 4 mm. The laser has a piezoelectric transducer attached to one of the cavity mirrors for operation at slightly different wavelengths.

Two germanium lenses, *L1* and *L2*, are used as a beam expander to obtain a 20-mm effective beam diameter. The use of a spatial filter (pinhole) was considered for cleaning up the beam. However, it is not desirable to put a thin metal pinhole near the converging point of lens *L1* since the high power density damages the pinhole. Also, aligning the pinhole for invisible radiation requires a special technique and care. Therefore, we actually overexpanded the beam at lens *L2* so that *L2* can pick up the rather uniform central portion of the Gaussian beam. The intensity at the edge of the beam at lens *L2* is  $\approx 70\%$  of that at the center. The final quality of the beam is reasonable for testing purposes.

There are two beam splitters: one made of germanium (BS1) and the other of zinc selenide (BS2). BS1 works as a reflector for the low-power He-Ne laser (which is expanded and aligned coaxially with the CO<sub>2</sub> laser for alignment purposes) and transmits the IR radiation to the subsequent beam paths. The zinc selenide beam splitter is chosen because it too is transparent at the 0.6328- $\mu\text{m}$  wavelength of the alignment He-Ne laser. Both beam splitters are 50 mm in diameter and 6 mm

C. R. Hayslett is with STEWS ID-O Instrument Directorate, White Sands Missile Range, New Mexico 88002; the other authors are with University of Arizona, Optical Sciences Center, Tucson, Arizona 85721.

Received 28 November 1979.

0003-6935/80/111862-08\$00.50/0.

© 1980 Optical Society of America.

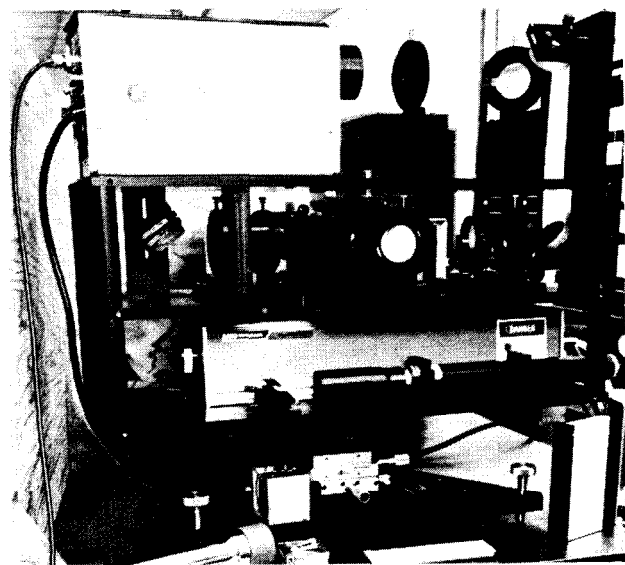
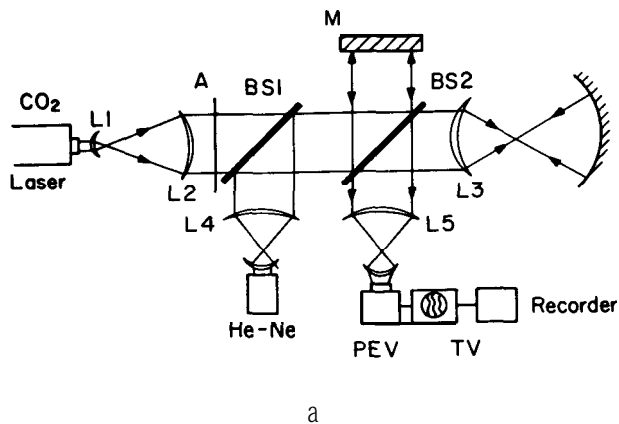


Fig. 1. Infrared Twyman-Green interferometer: (a) schematic; (b) photograph.

thick with enough wedge to avoid unwanted secondary reflections.

All the lenses are of the meniscus type fabricated for minimum third-order spherical aberration. As mentioned earlier,  $L1$  and  $L2$  are of germanium, and  $L3$  is of zinc selenide for both the IR and the He-Ne lasers.  $L5$  consists of a two-lens finite conjugate zooming system that images and magnifies the surface of the test optic onto the detector target. It provides a sharply defined image of the pupil and eliminates uncertainties caused by Fresnel diffraction.  $L4$  is an ordinary beam expander for the He-Ne laser.

The optical quality requirement for the components is most demanding for the reference mirror  $M$ , the major beam splitter  $BS2$ , and the diverger  $L3$ . While the spherical aberration introduced by a singlet diverger is acceptable for large  $f/Nos.$ , a singlet cannot be used for small  $f/Nos.$  For example, the spherical aberration for  $f/2.5$  diverger is about  $\lambda/3$  at  $10.6 \mu m$  for germanium optics. Therefore, we have to use either a doublet or an aspheric lens for faster divergers. Calcium fluoride

( $CaF_2$ ) plates  $A$  of different thickness have been used to control the incident flux onto the imaging detector. Nearly 30% of the energy is absorbed per 1-mm thickness of  $CaF_2$ .

Since IR radiation is invisible to human eyes, we need special techniques for the alignment. There are several IR, or heat sensing, materials that can be useful for this purpose. Liquid crystal paper was used at the earlier stages but was put aside immediately because of its poor resolution. Waxed paper and thermal image plates have been widely used. The thermal image plate has thermally sensitive phosphors that are fluorescent when illuminated by UV radiation, but the intensity of fluorescence decreases with increasing temperature. The thermal image plate has proved to be the most sensitive and handy tool throughout the alignment and testing procedures.

Recent advances in the area of IR detectors have made it possible to develop an IR interferometer. In particular, the pyroelectric vidicon<sup>5</sup> (PEV) is most useful as a detector for an interferometer working at  $10.6 \mu m$ . It does not need a cooling system and is compatible with the conventional TV format. However, since the PEV is sensitive only to time-varying changes in temperature at the scene, we have to modulate the intensity of the scene continuously.

There are several ways to introduce modulation of intensity on the target of a PEV. We tried mechanical chopping using blades, but putting a motor and a chopper onto the system caused extra complications in design and fabrication with possible unwanted vibration. Next we tried electrical chopping by dithering one of the cavity mirrors inside the  $CO_2$  laser head by use of the piezoelectric transducer. This allowed us to pick up slightly different longitudinal modes by varying the cavity length. These different modes introduce sufficient phase shift in the interferometric pattern to have effective modulation of the intensity on the target. Panning the camera head is another method. Likewise, using a piezoelectric transducer to dither the reference mirror, or introducing a small vibration into the whole system, including the optical bench, causes the fringes to shift sufficiently to produce the same effect as panning. However, all the above methods have a common drawback, i.e., they all show annoying blinking motion with changing phase of the interferometric pattern at the same frequency as the chopping or external vibration. Currently, we are synchronizing the PEV with the electrical modulation of the power of the laser output to obtain stable fringes with an optimum modulation frequency.

A conventional TV monitor and video recorder-player are used for display and later analysis of the interferometric patterns. The vidicon has  $>200 \times 200$  resolution elements. If the resulting interferogram contains, say, ten fringes, the fringe position can be measured to an average accuracy of  $1/20$  fringe, assuming the center of the fringe can be located within  $\pm 1$  pixel.

Typical interferograms obtained using the interferometer are shown in Fig. 2. Figures 2(a) and (b) show an interferogram of a germanium lens and an elliptical

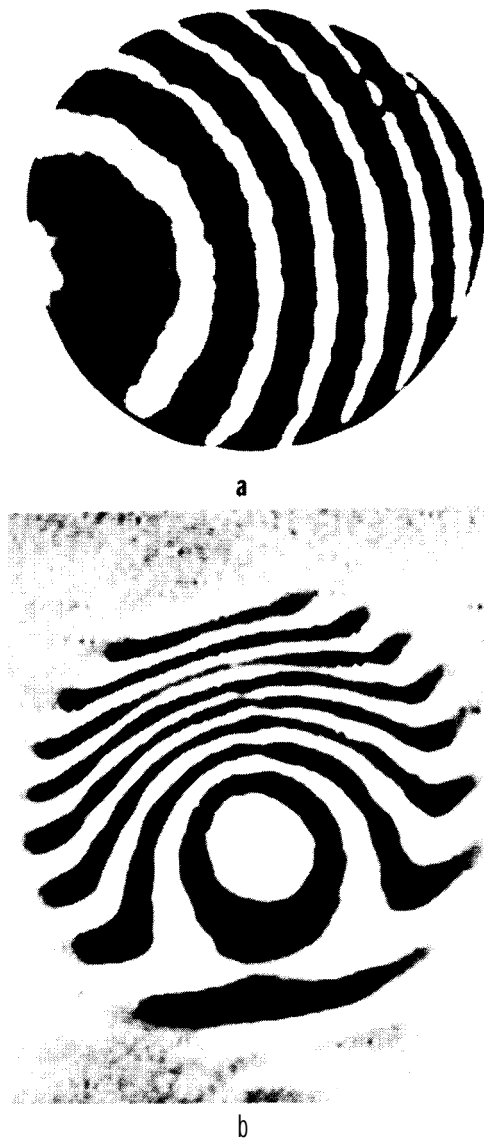


Fig. 2. Interferograms of (a) germanium lens of 2.54-cm (1-in.) diam and 12.5-cm (5-in.) focal length and (b) elliptical mirror of 5-cm (2-in.) diam and 7.5-cm (3-in.) focal length with conic constant of -0.5418.

mirror having 27- $\mu\text{m}$  departure from a best-fit sphere.

### III. Surface Roughness vs Fringe Contrast

#### A. Analysis

The measurement of rms surface roughness<sup>6</sup> can be done in many different ways. One approach is to observe the fringe contrast of the test surface using an interferometer. The fundamental analysis was shown by Munnerlyn and Latta.<sup>3</sup> The scattering theory of electromagnetic waves<sup>7</sup> says that the specular component of the scattered light increases with increasing wavelength for random rough surfaces. This fact enables us to do rough surface interferometry for the optically rough surfaces using a  $\text{CO}_2$  laser working at the 10.6- $\mu\text{m}$  wavelength. Figure 3(a) shows a simplified

schematic of a Twyman-Green interferometer for the rms roughness measurement.

As will be obvious later, the usefulness or the validity of this method is limited to the objects of surface irregularities that are small compared with the probing wavelength. Then the surface introduces only small phase changes in the wavefront. Figure 3(b) illustrates the random contour of a rough surface with surface height function  $h(x,y)$  and zero mean. After the reflection from the surface, the amplitude of the object wavefront is

$$U_o^+ = \rho_o U_o \exp\{i[2kh(x,y) + \alpha x]\}. \quad (1)$$

Similarly for a perfectly smooth reference mirror, the amplitude of the reference wavefront can be written as

$$U_r^+ = \rho_r U_r. \quad (2)$$

Here,  $k = 2\pi/\lambda$ , and  $\alpha$  is the relative tilt angle between the wavefront reflected from the reference flat and the wavefront reflected from the surface of the zero mean of the test object.  $U_o$  and  $U_r$  represent the incoming plane wavefront of constant amplitude from the expanded light source. Subscripts o and r refer to the object and reference wavefronts, respectively, and superscript + means the wavefronts after the reflections from both surfaces.  $\rho$  is the reflectivities of the materials of the reference flat and the test object.

Use of the Fourier optical analysis<sup>8</sup> of a coherent image forming system leads us to the final amplitudes of both interferometer arms at the image plane:

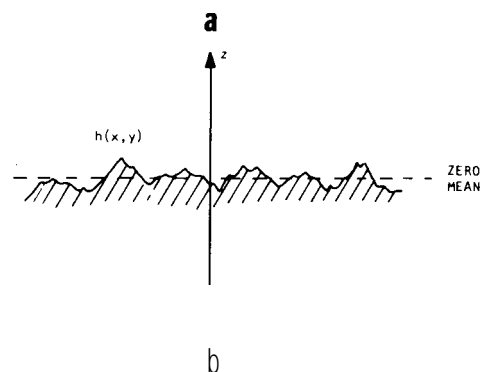
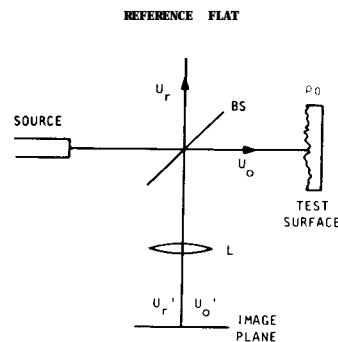


Fig. 3. Rough surface interferometry: (a) Twyman-Green interferometer with two image-forming lenses; (b) random surface profile of test object.

$$U_o = \tau q \left( x, y; \frac{1}{\lambda l} \right) \exp(ikz_o) \rho_o \exp[i\{2kh(x, y) + \alpha x\}] U_o, \quad (3)$$

$$U_r = \tau q \left( x, y; \frac{1}{\lambda l} \right) \exp(ikz_r) \rho_r U_r, \quad (4)$$

where  $\tau$  is the loss factor due to the reflection or absorption by the imaging lenses, and

$$q \left( x, y; \frac{1}{\lambda l} \right) \equiv \exp[i\pi(x^2 + y^2)/\lambda l]$$

is the quadratic phase related to the propagation of the wavefronts.  $l$  is the distance from the focal point of the imaging lens to the image plane.  $z_o$  and  $z_r$  are the distances between the image plane and the test object and reference flat, respectively. In the above equations, we neglected the geometrical factors, the magnification at the image plane, and the size of the aperture stop of the image forming system. Then, the image intensity distribution at the detector is given by

$$I = |U_o + U_r|^2. \quad (5)$$

The average image intensity distribution can be obtained assuming that the random intensity distribution at the image plane is ergodic, and the surface height distribution is Gaussian with a standard deviation  $\sigma$ .

The normal probability distribution function is then given by

$$p(h) = \frac{1}{(2\pi)^{1/2}\sigma} \exp\left(-\frac{h^2}{2\sigma^2}\right). \quad (6)$$

The ensemble average value  $\langle I \rangle$  is calculated as the spatial average over aperture  $A$  of the test surface:

$$\begin{aligned} \langle I \rangle &= \iint_A p(h) I(h) dh \\ &= \kappa \left[ 1 + \left( \frac{\rho_o}{\rho_r} \right)^2 \left( \frac{U_o}{U_r} \right) + 2 \left( \frac{\rho_o}{\rho_r} \right) \left( \frac{U_o}{U_r} \right) \cos(\alpha x) \right. \\ &\quad \left. \times \exp(-2k^2\sigma^2) \right], \end{aligned} \quad (7)$$

where  $\kappa = |\tau|^2 \rho_r^2 U_r^2$ . The contrast of the fringes is defined as

$$\begin{aligned} C &\equiv \frac{\langle I \rangle_{\max} - \langle I \rangle_{\min}}{\langle I \rangle_{\max} + \langle I \rangle_{\min}} \\ &= \frac{2(\rho_o/\rho_r)(U_o/U_r)}{1 + (\rho_o/\rho_r)^2(U_o/U_r)^2} \exp(-8\pi^2\sigma^2/\lambda^2) \\ &= C_o C_\sigma, \end{aligned} \quad (8)$$

where

$$\begin{aligned} C_o &= \frac{2(\rho_o/\rho_r)(U_o/U_r)}{1 + (\rho_o/\rho_r)^2(U_o/U_r)^2}, \\ C_\sigma &= \exp(-8\pi^2\sigma^2/\lambda^2). \end{aligned} \quad (9)$$

Therefore, the resulting contrast is the product of the contrast of the perfectly smooth surface  $C$ , and that of degrading factor  $C$ , due to the scattering by the random rough surface. If we adjust the incoming amplitudes  $U_o$  and  $U_r$  to have unit contrast for  $C_o$ , the final result becomes

$$C = C_\sigma = \exp(-8\pi^2\sigma^2/\lambda^2). \quad (10)$$

## B. Experiments

Samples of glasses were ground with aluminum oxide of different average particle sizes. The fringe contrasts were measured by reading the average intensity distribution on the PEV target in terms of voltages registered on the oscilloscope. PEV is known to have good linear response<sup>9</sup> if measured before the amplifier. However, since the pedestal level of the PEV can be set arbitrarily, the absolute readings of the average maximum values of the fringes do not produce direct values of contrast. Therefore, the values of contrast for the rough surface samples were normalized with respect to that of the perfect surface.

In Fig. 4 we have (a) the mechanical readings of the profiles of surface irregularities using a Talystep, (b) the electronic readings of the interferometric patterns, and (c) the photographic pictures of the fringes taken through a TV monitor. The comparisons of the contrasts of the fringes and the standard deviations of surface roughness obtained by Talystep and interferometric measurements are listed in Table I. As shown in Table I, the standard deviations obtained from the interferometric measurements of the fringe contrasts are in good agreement with the values obtained by mechanical Talystep measurements of the rough surface samples within a few percent. The contrast of fringes drops significantly for the samples of standard deviation  $>1/4 \lambda$  at  $10.6 \mu\text{m}$ . Figure 5 illustrates the theoretical and experimental results of the relationship between contrast  $C_o$  and scaled roughness  $a/\lambda$ .

## IV. Applications

The following examples show the usefulness and effectiveness of the long-wavelength interferometric system for the testing of special optics demanded in recent years in the areas of high energy laser systems and modern astronomical telescopes or tracking systems. First, in Fig. 6 we have interferograms of diamond-turned spherical metal mirrors plated with aluminum or copper. Both mirrors were tested at  $0.6328$  and  $10.6 \mu\text{m}$ , respectively. The interferograms show us the effects of the reduced sensitivity and the increased specular components from the rough surfaces at the longer wavelength.

Second, a large off-axis parabolic collimator mirror is being fabricated at the Optical Sciences Center. A drawing of the mirror is shown in Fig. 7. The mirror has a vertex radius of  $12.8 \text{ m}$  and an effective clear aperture of  $1.22 \text{ m}$ . The departure from the best-fit reference sphere, which is tangent to the parabola at its vertex, is  $260.6 \mu\text{m}$ . Even if we choose a reference sphere of longer radius and then tilt that sphere in the plane of the offset of the parabolic segment, the departure is  $116.8 \mu\text{m}$ . In either case, an impractical amount of time and money are required to achieve the final surface figure by optical polishing only. Therefore, to speed up the fabrication, a sequence of grinding steps has to be done starting with fine grades of abrasive (9- or  $12\text{-}\mu\text{m}$  grit) until any optical polishing is possible. This brings us to the most crucial part of the fabrication, i.e., the testing of the large nonreflective rough surface

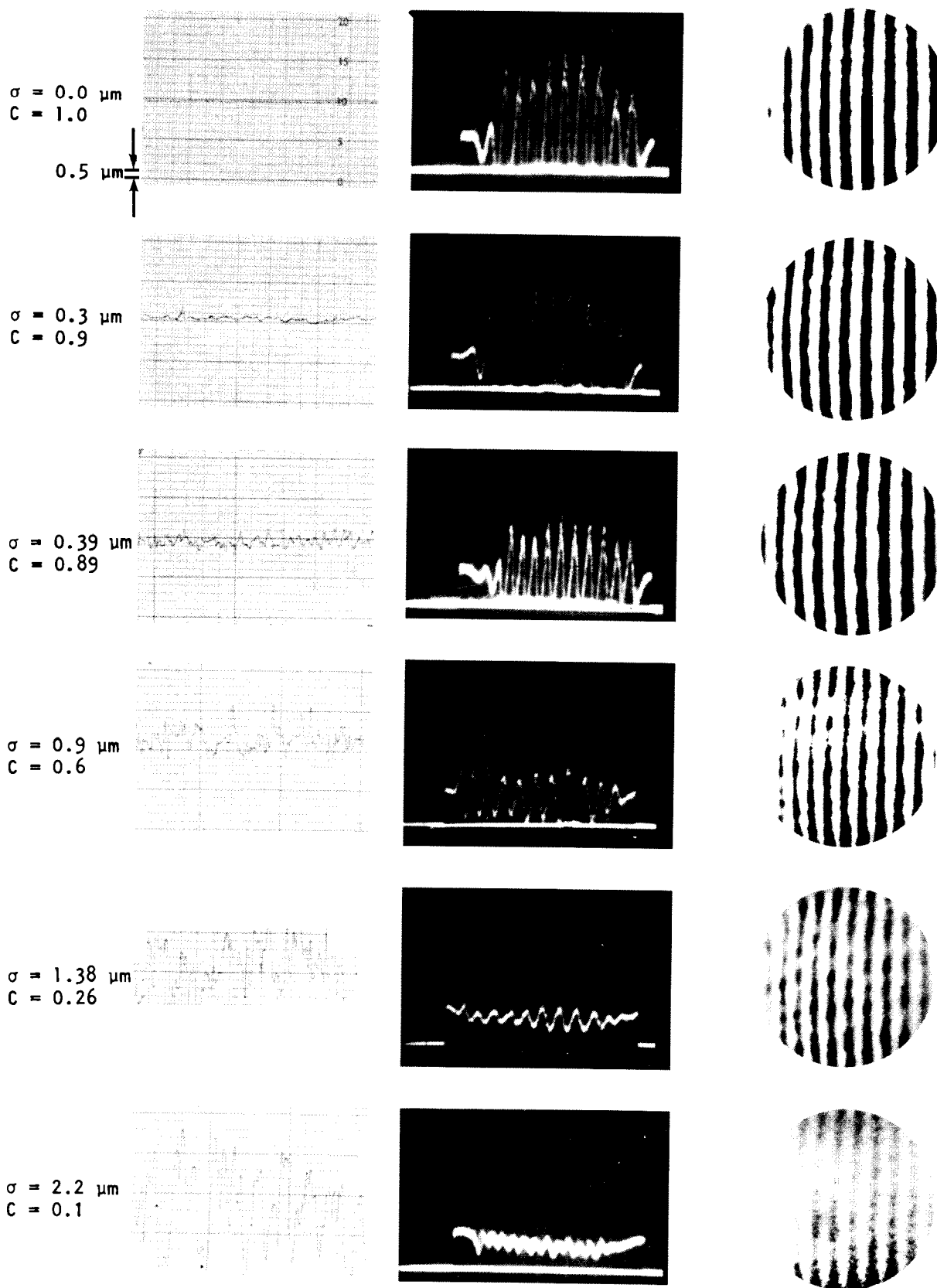


Fig. 4. (a) Talystep readings of glass samples; (b) oscilloscope readings of interferometric fringes; (c) photographic pictures of fringes taken through a TV monitor.

Table I. Results of Fringe Contrasts vs Standard Deviations

Sample	Average grit size ( $\mu\text{m}$ )	Talystep readings		Interferometric readings	
		Standard deviation $\sigma$ ( $\mu\text{m}$ )	Contrast $C_\sigma$ [from Eq. (10)]	Contrast, $C_\sigma$	Standard deviation $\sigma$ ( $\mu\text{m}$ ) [from Eq. (10)]
<i>a</i>	(Polished)	0	1	1	0
<i>b</i>	3	0.28	0.94	0.93	0.32
<i>c</i>	12	0.39	0.89	0.87	0.44
<i>d</i>	25	0.89	0.57	0.54	0.93
<i>e</i>	40	1.38	0.26	0.23	1.44
<i>f</i>	63	2.22	0.05	0.07	1.95

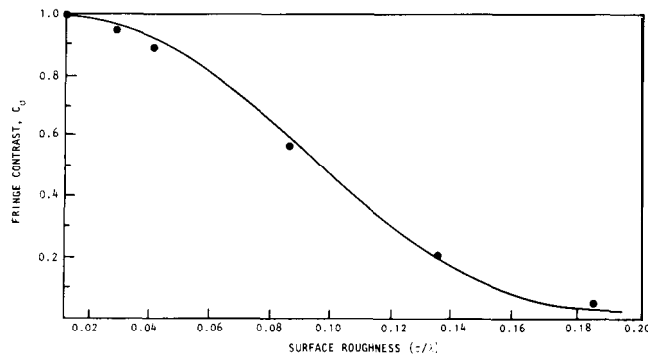


Fig. 5. Comparison of scaled rms roughness and values of contrast obtained from Talystep readings and interferometric measurements.

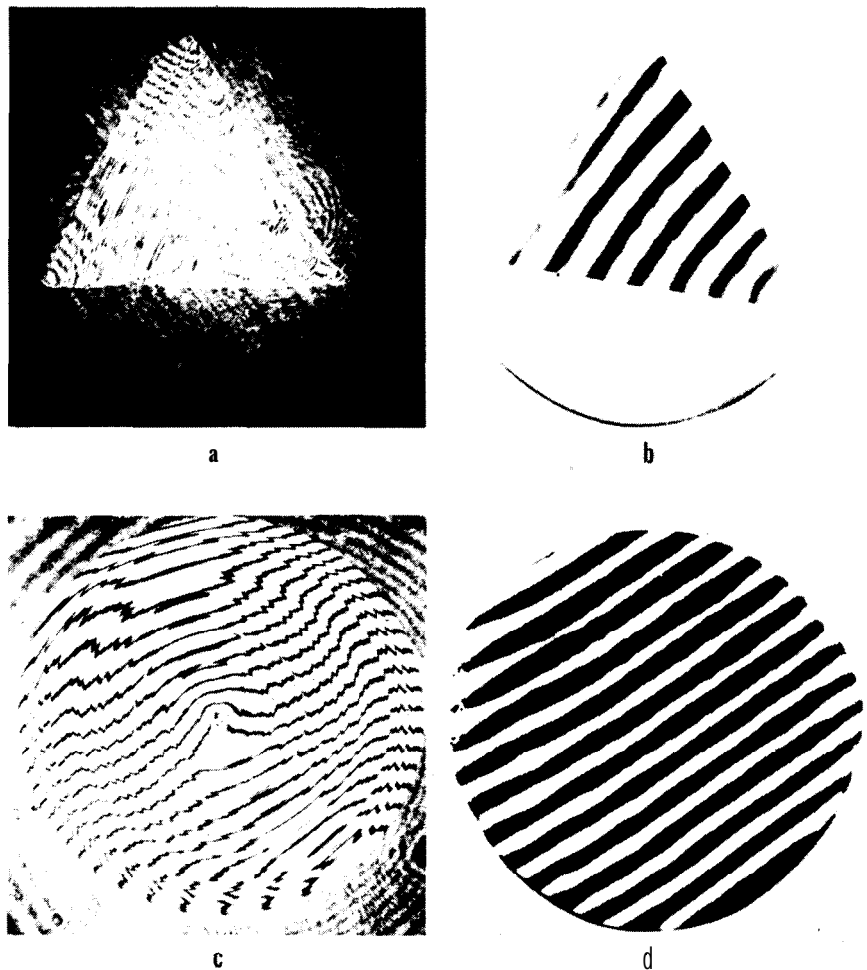


Fig. 6. Interferograms of diamond-turned spherical metal mirrors coated with aluminum (a), (b) and copper (c), (d) at  $0.6328 \mu\text{m}$  (a), (c) and at  $10.6 \mu\text{m}$  (b), (d).

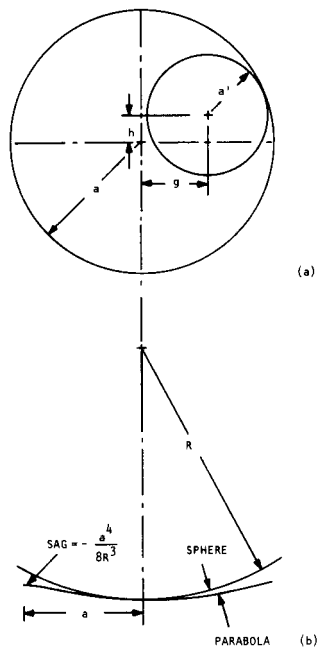


Fig. 7. Off-axis parabola: (a) segment from a large on-axis parabola.  $a = 1.73$  m,  $a' = 0.71$  m,  $h = 0$ , and  $g = 1$  m. (b) Departure from best-fit sphere.  $R = 12.8$  m.

mirror. The results given in Table I show that a  $10.6\text{-}\mu\text{m}$  interferometer can be used to obtain fringes of reasonable contrast for the testing of surfaces ground with 9- or  $12\text{-}\mu\text{m}$  grit.

In Fig. 8 we have a layout of the reflective null test of the off-axis parabola using a large reference flat  $M_2$ . The flat is used both to autocollimate the parabola as well as to fold the focus of the parabola to the vertex of the symmetric parabola surface. It is a double pass setup in which the beam is reflected off the flat and the parabola. Light from the vertex is folded by flat  $M_1$  so that it appears to be coming from the focus of the parabola. The light fills the parabolic mirror after flat  $M_2$  and is collimated. This column of light is reflected by flat  $M_2$  back to the parabola, which in turn refocuses the light toward its focus. The final reflections off flats  $M_2$  and  $M_1$  bring the light to focus at the mirror vertex where the wavefront is determined using the interferometer. Because the test is double pass off the parabola, a  $X/4$  peak-to-valley surface error appears as a full fringe error in the interferogram.

The double scattering off the parabola causes a problem. Even with the built-in He-Ne alignment laser, it is difficult to align the system because the visible light is scattered off the rough surface of the mirror and gives no appreciable return beam back to the interferometer. Obviously the double pass makes it even worse. Several methods have been attempted to overcome this problem in alignment. Fortunately, nature gives us one simple solution, beeswax. A small amount of beeswax is applied to the central portion of the parabola and is scraped off with a sharp razor blade. Then the coated portion of the surface has better reflectivity. Though our original He-Ne laser has served well for the testing of polished surfaces or other metallic surfaces of high

reflectivity, it does not have enough power for the present beeswaxed rough surface. Therefore, a secondary He-Ne(II) laser with higher power was adopted to assist the primary He-Ne(I) laser. The following is a brief summary of the alignment procedures.

Aim and focus alignment telescope  $A$  on vertex  $Q$  of the parabola without folding mirror  $M_1$  and locate the image of vertex  $Q$  on the center of the cross hairs.

Place folding mirror  $M_1$  and put an aperture stop  $S$  on the position where the image of the aperture falls on the center of the cross hairs of the alignment telescope. Then the aperture on the pinhole becomes the conjugate image point of vertex  $Q$  with respect to  $M_1$ . Remove the alignment telescope and put a  $45^\circ$  prism  $P$  behind the pinhole. Adjust the secondary He-Ne(II) laser and prism  $P$  so that the beam falls on the center of the parabola, where the beeswax was applied and scraped off previously, through the pinhole and mirrors  $M_1$  and  $M_2$ .

Adjust flat  $M_2$  and the parabola to have the return beam superposed upon the pinhole.

Remove prism  $P$  and the secondary He-Ne(II) laser.

Turn on the primary He-Ne(I) laser, which was aligned coaxially with the  $\text{CO}_2$  beam previously. Adjust the interferometer so that the primary He-Ne(I) beam passes through the pinhole and falls on the center of the parabola.

Turn off the He-Ne(I) laser and open up the aperture of stop  $S$ , then turn on the  $\text{CO}_2$  laser beam. Fringes are seen through the TV monitor, and the proper amount of tilt and defocus can be introduced to obtain the desired interferograms.

It normally takes less than half an hour for the above alignment procedure.

In addition, due to the judicious design of the polishing machine, the test is performed in situ. In other words, the mirror is not removed from the polishing machine, but rather the table of the machine is tipped over so that the mirror axis is horizontal. A sling mount

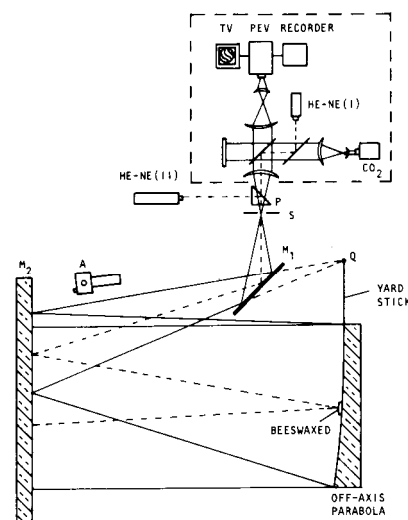


Fig. 8. Layout of testing of off-axis parabola.

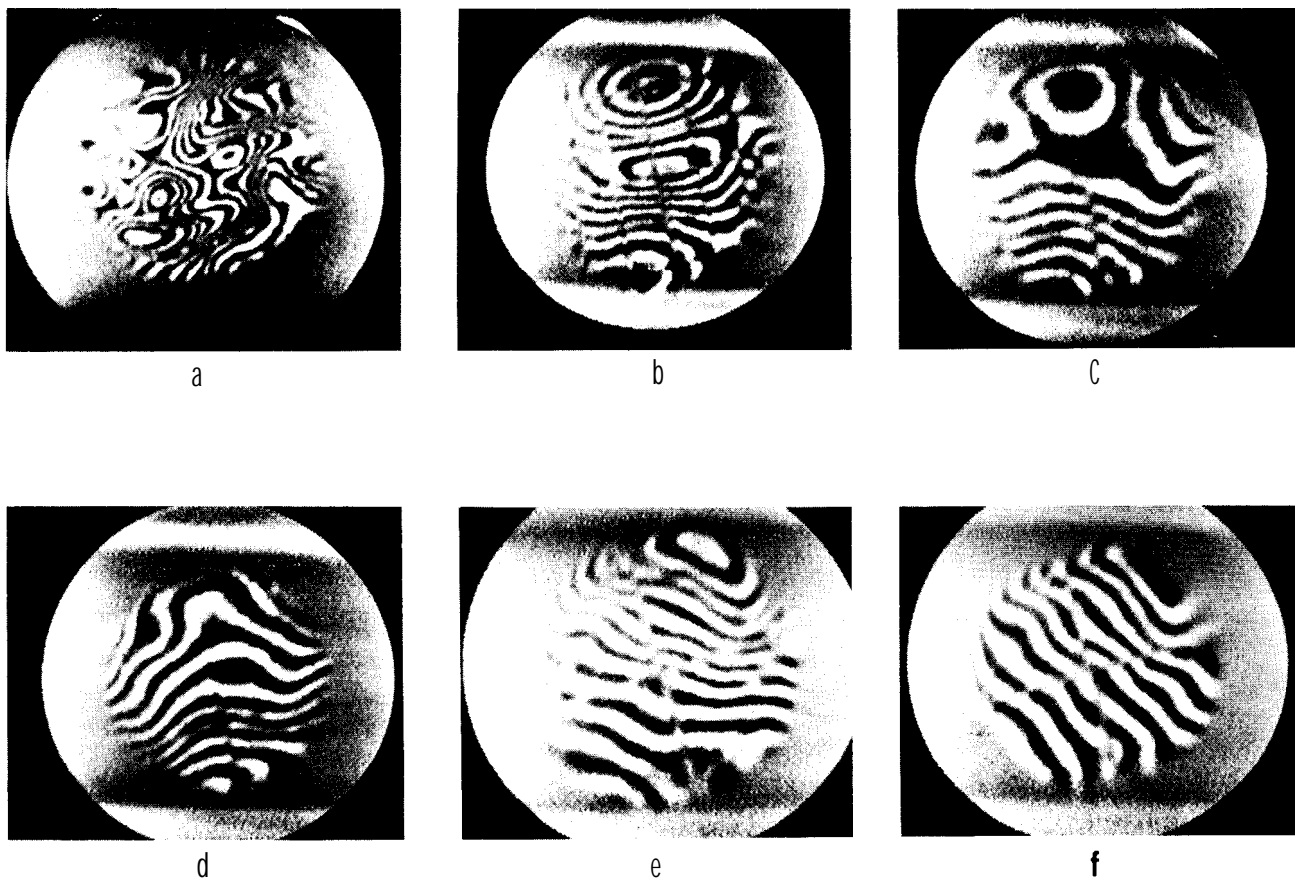


Fig. 9. Infrared interferograms of unpolished off-axis parabola in chronological order.

is built into the polishing machine table to support the mirror during the test exactly as it would be during use. Only a minimum amount of effort to realign the mirror in either the test or on the machine is required because the mirror is never moved off the machine. It is simply tipped up for test and is returned to a horizontal position for further work in figuring. Also, the interferometer unit can be brought to the predetermined position to save time and labor. In this manner, the turnaround time for testing is reduced significantly, and we can eliminate the hazards involved in realignment and handling the large pieces of glass. Therefore, this *in situ* test practically gives closed-loop feedback to the optician doing the figuring.

In Fig. 9 a series of interferograms obtained during the preliminary figuring by grinding is shown in chronological order.

## V. Conclusions

Our practical experience with IR interferometric systems has shown the usefulness and the effectiveness of long-wavelength interferometers in the fabrication and testing of certain optical components demanded in recent years. The extended capabilities to test the IR optics, diamond-turned metal mirrors, aspherics, and rough surface optics certainly help us to fabricate the modern optical components effectively and economically in the future.

The authors wish to thank R. E. Parks and T. Turner, Jr., of the Optical Sciences Center for valuable help and discussions during the alignment and test. This work was partially funded under contract DAAD07-77-C-0074 by the U.S. Army, White Sands Missile Range, New Mexico.

## References

1. O. Kwon et al., *J. Opt. Soc. Am.* 67,1305 (1977).
2. O. Kwon et al., *Opt. Lett.* 3, 118 (1978).
3. C. R. Mummerlyn and M. Latta, *Appl. Opt.* 7,1858 (1968).
4. W. L. Wolfe and G. J. Zisis, Eds., *Infrared Handbook* (Office of Naval Research, Department of the Navy, Washington, D.C., 1979), pp. 7-40.
5. T. Conklin and E. H. Stupp, *Opt. Eng.* 15,510 (1976).
6. J. M. Bennett, *Appl. Opt.* 15,2705 (1976).
7. P. Beckmann and A. Spizzichino, *Scattering of Electromagnetic Waves from Rough Surfaces* (Macmillan, New York, 1963), Chap. 5.
8. J. D. Gaskill, *Linear Systems, Fourier Transforms, and Optics* (Wiley, New York, 1978), Chap. 11.
9. B. Kazan, Ed., *Advances in Image Pickup and Display, Vol. 3* (Academic, New York, 1977), Chap. 1.